Sensors & Actuators: A. Physical 338 (2022) 113453

Contents lists available at ScienceDirect

Sensors and Actuators: A. Physical

journal homepage: www.journals.elsevier.com/sensors-and-actuators-a-physical

Open-loop control of electrostatic levitation actuators to enhance the travel-range of optical switches

Mohammad Mousavi [a], Mohammad Alzgool [a], Daniel Lopez [b], Shahrzad Towfighian [a,*]

[a] Binghamton University, 4400 Vestal Parkway East, Binghamton, NY 13902, USA
[b] The Pennsylvania State University, University Park, PA 16802, USA

ARTICLE INFO

Keywords:
Electrostatic levitation
MEMS
Actuators
Fringe field effect
Optical micro-mirrors
Large range
Command shaping
Open-loop control

ABSTRACT

Command shaping is a driving technique for handling the large settling time of the high-Q-MEMS actuators. The strong nonlinearity due to the electrostatic actuation limits the linear operation range in cantilevered or torsional micro-mirrors where command shaping techniques can be applied for positioning. Experimental and simulation results of this research demonstrate the effectiveness of using electrostatic levitation to overcome the actuation nonlinearities and a significant increase in the operation range. The motivation for this research is that applying the nonlinear command shaping causes complexity in command manipulation and requires an accurate knowledge of the nonlinear terms involved in the system model. The large linear operation range generated by the levitating force allows using the practical simple command shaping methods for open-loop control.

1. Introduction

Precise control of the dynamic and static state of a mechanical system is a critical mission for specific applications such as optics [1–4]. It is particularly important in micro electromechanical system (MEMS), i.e., micro-meter size devices with mechanical and electrical components.

The gap-closing configuration is the most well-known actuation device in MEMS systems where an electrical potential between a movable electrode and a fixed electrode results in the mechanical motion (also called capacitive or gap-closing mechanism). When the movable electrode gets close to the fixed electrode, the movable electrode becomes unstable and accelerates toward the fixed electrode. This phenomenon is called pull-in instability [1], which happens when the system state enters an unstable region and the system cannot find an equilibrium point to oscillate around or settle on. When the velocity or displacement of the movable electrode exceeds some thresholds, the pull-in instability occurs. In some MEMS applications such as MEMS RF switches, pull-in instability is considered as a useful feature, while in others, it is an undesirable feature that causes malfunctioning or permanent failure. Moreover, inside the pull-in instability region, the input/output relationship is highly nonlinear, which significantly complicates the implementation of dynamic control techniques. Such a nonlinearity impedes the application of MEMS as an actuator. Open-loop and closed-loop techniques have been suggested to drive the MEMS actuators.

A solution for driving micro-systems is feedback control, that is, reaching a desired system state automatically by manipulating the system inputs using sensors that provide information about the system state. Minimization of the settling-time as the required period to reach the desired state, overshoot, and the deviation from the desired state are the primary goals of feedback control. The main difference between feedback control and other control methods is the utilization of sensors to measure the system state during the operation and using the measurement data in the control algorithm in real time. Then, the measurement is transferred to a processing unit where the control algorithm manipulates a command signal according to the mathematical criteria of the design. One of the most important parameters of an analog input or output system is the rate at which the measurement device samples an incoming signal or generates the output signal. The sampling rate is the speed at which a device acquires or generates a sample. A fast input sampling rate acquires more points in a given time and can form a better representation of the original signal than a slow sampling rate. MEMS resonators are considered as fast dynamical systems with the fundamental frequencies in the order of kilo to mega Hertz. For a robust competent control of a MEMS oscillator, the hardware, which includes sensors, processing unit, and digital-to-analog and analog-to-digital data acquisition is required to meet the high-frequency system control

* Corresponding author.
E-mail addresses: smousav1@binghamton.edu (M. Mousavi), malzgoo1@binghamton.edu (M. Alzgool), ovl5064@psu.edu (D. Lopez), stowfigh@binghamton.edu (S. Towfighian).

https://doi.org/10.1016/j.sna.2022.113453
Received 4 October 2021; Received in revised form 7 February 2022; Accepted 13 February 2022
Available online 17 February 2022

requirements. Therefore, compared to the macro-scale dynamic systems, MEMS devices need more complex circuits and electronics. To avoid the aforementioned complications, the open-loop control is preferred instead of feedback control in some applications such as optical actuators.

Considering high quality factor MEMS actuators, open-loop control via command shaping for the purpose of static displacement is widely used among researchers [5–8–11,12,13]. During the switching between two positions, a smooth quasi-static motion is desired. Normally, formation of a motion using a voltage pulse takes a considerable time because the undesired oscillations should fade. Researchers have shown how command shaping techniques allow for activation and deactivation of a specific mode of continuous systems. In [8,11–13], they used MEMS oscillators for static displacement and showed a perfect ringing and settling-time reduction.

For nonlinear input/output micro-systems, such as micro-mirrors and cantilevered parallel-plate actuators, zero-velocity and zero-velocity-and-derivative fail to function properly. To address this issue, a nonlinear command shaping scheme was presented for electromagnetic actuators [14,15]; however, neglecting the damping effect undermines the effectiveness of this method. Another nonlinear scheme was offered for command shaping in an electrostatic torsional micro-mirror [16]. The results are worthwhile in the matter of the settling-time and handling the nonlinearities. Nonlinear schemes are complicated compared to linear schemes and require an accurate knowledge of the nonlinear input/output relationship, which itself demands a perplexing experimental and simulation process.

Beside the powerful features of MEMS parallel-plate configuration such as low energy requirement, there are some shortcomings that cast a shadow over their popularity. The parallel-plate configuration suffers mostly from the small range of motion as there is only a small gap between the electrodes and only one-third of the initial gap is usable due to the pull-in instability. One may plan to increase the initial gap to solve this problem. Unfortunately, the initial gap cannot be large because the parallel-plate capacitive force is reduced with the gap.

As a replacement for the gap-closing actuation, some researchers studied the electrostatic fringe field [17–20,21] for actuation. This effect was implemented as a mechanism for generating attractive force [22] by surrounding the movable electrode by two electrodes, while the center electrode was removed in this research. Adding a center electrode creates asymmetry in the electrostatic field and changes the attractive force to the repulsive one [20,23–25]. In the latter mechanism, the movable electrode is made of polysilicon. The simulation results show that the movable electrode should be a conductor, and any dielectric layer on the movable electrode limits the electric field lines and produces an attractive force. Compared to the gap-closing mechanism, the dependence of the fringe field force on the movable electrode position is significantly smaller. In a wide region of motion, the fringe field force can be considered as a constant force, while in the gap-closing actuation, the electrostatic force becomes unmanageable when the movable electrode is situated in the proximity of the driving electrode. As mentioned, adding the center electrode and the surrounding electrodes results in the electrostatic force to be applied in the opposite direction of the substrate. Therefore, use of the side electrodes no longer restricts the beam motion. The generated repulsive force is called levitating force or fringing electrostatic force in the literature. As reported in [26], a 500 μm cantilever can be raised more than 30 μm which is 27 times larger than the maximum amplitude enabled by the parallel-plate mechanism. Compared to conventional parallel plates, this method requires a larger voltage to consume (~ one order of magnitude). However, implementation of the levitation actuators enables high-amplitude motion, smaller nonlinearities, pull-in free operation, tunability and high scanning speeds, which are desirable for optical scanning and filtering applications. The features of tunability and high speed originate from the fact that the electrostatic levitation causes a stiffening effect on the resonator and therefore, increases the frequency up to 10% with the increase of the side voltage [19].

Despite the merits of the levitation-based MEMS for long range operation, the command shaping has never been applied to it. In this study, we characterize the behavior of an electrostatic levitation MEMS actuator response to a command shaping technique, which can have a wide range of applications in optical switches and filters. A micro-cantilever is actuated simultaneously by the gap-closing mechanism and levitating force mechanism. By using a micro-cantilever as the actuator movable electrode, we intended to simulate a picture of how the levitation mechanism can improve the actuation of the micro-mirrors for applications in confocal microscopy, projection displays and optical coherence tomography. The introduction is followed by a mechanical description (Section 2). A model that is consistent with the static and dynamic experiments is provided in the mathematical modeling (Section 3). Then, in the experimental setup section (Section 4) we describe the necessary procedures and the apparatus for conducting the tests. The results are then summarized in Conclusions (Section 6).

2. Mechanism description

A micro-cantilever as the movable electrode is anchored above a fixed center electrode in parallel with the gap of d (Fig. 1). At the same height with the center electrode, two side electrodes are fabricated for inducing levitating force. As a result of the side electrodes, a strong electrostatic fringe field surrounds the movable electrode and pulls it away from the substrate. The side electrodes are inputted using a DC voltage named levitating voltage V_L in this paper. The center electrode is charged using the driving voltage V_D which applies an attractive force between the parallel plates and controls the movable electrode motion. The characterization of the levitation MEMS has been investigated in [19,20].

3. Mathematical modeling

3.1. Levitation-based MEMS model

The movable electrode is a fixed-free beam and is modeled using Euler-Bernoulli beam theory [27].

$$\rho A \frac{\partial^2 w}{\partial t^2} + c\frac{\partial w}{\partial t} + EI\frac{\partial^4 w}{\partial x^4} = f(w,x,t) \tag{1}$$

where $A = b_3 h_1$ and $f(w, x, t)$ denote the beam cross-sectional area and the electrostatic forces, respectively. The micro-cantilever is a continuous system with four boundary conditions. Therefore, the absolute transverse displacement can be modeled as a summation of distinct components named as modes. Each mode has a mode shape with respect to the system boundary conditions. Because each component satisfies the equation of motion and the boundary conditions, they can be analyzed separately. Galerkin's method is a discretization method that simplifies the system's partial differential equation by approximating it as a set of ordinary differential equations. The results show that the contribution of the first mode in the absolute displacement is significantly larger than the other modes. Therefore, the micro-cantilever is approximated using the first mode as follows Table 1.

$$w(x,t) \approx \phi(x)q(t) \tag{2}$$

where $\phi(x)$ and $q(t)$ are the first shape function and the separated

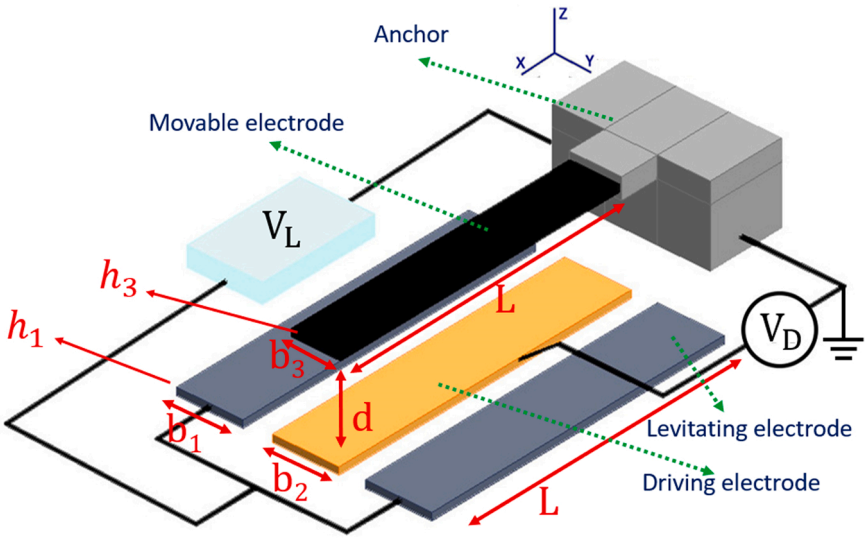

Fig. 1. Levitation MEMS actuator. The cantilever is grounded, electronically connected to the anchor. The geometric parameters are addressed in Table 1.

Table 1
Micro-actuator properties and geometry.

Parameter	Symbol	Value
Beam Length	L	$505\mu m$
Beam Width	b_3	$20.5\mu m$
Beam Thickness	h_3	$2\mu m$
Module of Elasticity	E	$160GPa$
Density	ρ	$2330kg/m^3$
Initial Gap	d	$2\mu m$
Bottom Electrode Width	b_2	$32\mu m$
Side Electrode Width	b_1	$28\mu m$
Electrode Thickness	h_1	$0.5\mu m$
Dimple Height	h_d	$0.75\mu m$

time function, respectively. Then, Eq. 2 is substituted into Eq. 1 to obtain the set of ODE's as,

$$\phi\frac{d^2q}{dt^2}+c\phi\frac{dq}{dt}+\frac{d^4\phi}{dx^4}q=+f(\phi q,x,t) \tag{3}$$

Considering the orthogonality of the mode shapes, Eq. 3 is multiplied by $\phi(x)$ and then integrated over the length of the beam.

$$\int_0^L\phi^2dx\frac{d^2q}{dt^2}+c\int_0^L\phi^2dx\frac{dq}{dt}+q\int_0^L\frac{d^4\phi}{dx^4}\phi dx=\int_0^L\phi f(\phi q,t)dx \tag{4}$$

One shape function is used to discretize the system equation Eq. 1 as in Eq. 2.

$$m\frac{d^2q}{dt^2}+cm\frac{dq}{dt}+kq=F(q,V_D,V_L) \tag{5}$$

where,

$$m=\int_0^L\phi^2dx \tag{6}$$

$$k=\int_0^L\frac{d^4\phi}{dx^4}\phi dx \tag{7}$$

Using the experimental data and logarithmic decrements method, the quality factor was obtained $Q=200$. As verified in [19], the Galerkin's reduced order method is used to obtain the discrete form of the nondimensional beam partial differential equation that satisfies $\phi(0)=0$, $\phi'(0)=0$, $\phi''(L)=0$, $\phi\prime\prime'(L)=0$:

$$\phi(x)=cosh\,\theta x-cos\,\theta x+0.7341(sinh\,\theta x-sin\,\theta x) \tag{8}$$

According to the COMSOL results [19] the electrostatic force of the center and levitation electrodes is made up of three parts as in the Eq. 1. Considering the first cantilever mode shape, θ is equal to $1.875/L$ in Eq. 8. Substituting Eq. 8 into the right side of Eq. 4 gives,

$$F(q,V_D,V_L)=F_L(q,V_L)+F_{LD}(q,V_D,V_L)+F_D(q,V_D) \tag{9}$$

The pure levitating part is estimated as a polynomial as:

$$F_L(q,V_L)=V_L^2\sum_{j=0}^{9}a_jq^j \tag{10}$$

The interaction between the levitation and driving electrodes is estimated as:

$$F_{LD}(q,V_L,V_D)=V_LV_D\sum_{j=0}^{9}b_jq^j \tag{11}$$

The attractive force of the driving voltage is represented as:

$$F_D(q,V_D)=V_D^2\frac{a}{(q+d)^{2.15}} \tag{12}$$

The coefficients a_j and b_j and a are shown in Table. 2.Table. 3.

3.2. Double-step command shaping

As in Eq. 5, the reduced-order system dynamics is a second-order

Table 2
The electrostatic force coefficients of a cantilevered levitation MEMS actuator obtained from COMSOL simulations.

Parameter	Value	Parameter	Value
a_0	2.48×10^{-7}	b_0	2.16×10^{-7}
a_1	9.3×10^{-3}	b_1	-9.78×10^{-2}
a_2	-3.44×10^{3}	b_2	1.64×10^{4}
a_3	3.13×10^{8}	b_3	2.15×10^{9}
a_4	-1.06×10^{13}	b_4	2.28×10^{14}
a_5	-5.79×10^{17}	b_5	-1.79×10^{19}
a_6	7.78×10^{22}	b_6	9.43×10^{23}
a_7	-3.47×10^{27}	b_7	-3.09×10^{28}
a_8	7.29×10^{31}	b_8	5.64×10^{32}
a_9	6.08×10^{35}	b_9	-4.38×10^{36}
a	-1.57×10^{-8}		

Table 3
Levitation-based MEMS parameters and properties.

Parameter value	Symbol
Beam Length	505 μm
Beam Width	20.5 μm
Beam Thickness	2 μm
Module of Elasticity	160 GPa
Density	2330 kg/m^3
Initial Gap	2 μm
Driving electrode width	32 μm
Levitating electrode width	28 μm
Fixed Electrode Thickness	0.5 μm

linear system with nonlinear actuation $F_e(q, t)$. The linear double-step command shaping procedure is illustrated in Fig. 4. First, the operation range R is defined by the user. Using the static displacement graph, the movable electrode must be levitated at $q = q_0$ where the distance from the center electrode is $g = d + q_0$. As will be shown in Fig. 8, the side voltage V_L is the required voltage to levitate the movable electrode at $q = q_0$. In other words, q_0 is the initial position of the movable electrode that considers the required operation range R. q_0 is selected in a way that it allows the gap-closing mechanism to sweep in the range of R. The displacement with respect to the levitated position is denoted by δ that is considered as the distance driven by the user that uses the gap-closing mechanism.

$$\delta(t) = q(t) - q_0 \tag{13}$$

Expansion of the electrostatic force Eq. 5 around the levitated position q_0 using the Taylor series gives:

$$F(q, V_D, V_L) = F(q_0, V_{L,R}, V_D) + \frac{\partial F(q_0, V_{L,R}, V_D)}{\partial q}\delta + \ldots \approx F_e - k_e\delta \tag{14}$$

where the only first two terms are considered. The levitating voltage, $V_{L,R}$ is the voltage that lifts the beam and q_0 is the corresponding equilibrium position. We then keep the levitating voltage constant and change the driving voltage, V_D for the double step operation. The linear force approximation is denoted by F_e, which becomes a function of V_D only. Using Eqs. 10,11,12), F_e and k_e are calculated as:

$$F_e(V_D) \approx F(q_0, V_{L,R}, V_D) = V_{L,R}^2 \sum_{j=0}^{9} a_j q_0^j + V_{L,R} V_D \sum_{j=0}^{9} b_j q_0^j + V_D^2 \frac{a}{(q_0 + d)^{2.15}} \tag{15}$$

$$k_e \approx -\frac{\partial F(q_0, V_{L,R}, V_D)}{\partial q} = -\left(V_{L,R}^2 \sum_{j=1}^{9} j a_j q_0^{j-1} + V_{L,R} V_D \sum_{j=1}^{9} j b_j q_0^{j-1} - V_D^2 \frac{2.15a}{(q_0+d)^{3.15}}\right) \tag{16}$$

Rewriting Eq. 5 with $\delta(t)$ as the variable gives:

$$m\frac{d^2(\delta + q_0)}{dt^2} + cm\frac{d(\delta + q_0)}{dt} + k(\delta + q_0) = F_e - k_e\delta \tag{17}$$

As previously mentioned, q_0 is a constant value defined by the user. Eq. 17 is simplified to:

$$m\frac{d^2\delta}{dt^2} + cm\frac{d\delta}{dt} + (k + k_e)\delta = F_e - kq_0 \tag{18}$$

As in Eq. 17, F_e is considered as a driving force that is independent from the cantilever position and varies with only V_L and V_D. k_e is the nonlinear effect of the electrostatic force that results in a shift in the fundamental frequency.

For control purposes, the movable electrode is initially levitated by V_L while no driving voltage is applied. As a result, the beam is raised to $q = q_0$. Therefore, the static force balance Eq. 5 at the initial state is $F_L(q_0, V_L) = kq_0$.

Using the mentioned equation and substituting Eqs. (15,16) in Eq. 18, the linear governing dynamics Eq. 5 are reduced to:

$$m\frac{d^2\delta}{dt^2} + cm\frac{d\delta}{dt} + (k + k_e)\delta = B_1 V_D^2 + B_2 V_D = \widetilde{F}(V_D) \tag{19}$$

where B_1 and B_2 are the driving force constants defined in the following:

$$B_1 = \frac{a}{(q_0 + d)^{2.15}} \tag{20}$$

$$B_2 = V_L \sum_{j=0}^{9} b_j q_0^j \tag{21}$$

and $\widetilde{F}(V_D)$ is the driving force as a function of the driving voltage V_D only which makes Eq. 19 a linear system with linear force response. The frequency shift due to the nonlinear force is important information for the command shaping process as the command timing depends on the step response of the system. Using the Jacobian matrix of the second-order system Eq. 19, the free-oscillation frequency of the system is calculated in the following. Representing Eq. 19 in state-space form gives:

$$\begin{pmatrix} \frac{d\delta}{dt} \\ \frac{d^2\delta}{dt^2} \end{pmatrix} = \begin{pmatrix} 0 & 1 \\ -(k + k_e)/m & -c \end{pmatrix} \begin{pmatrix} \delta \\ \frac{d\delta}{dt} \end{pmatrix} \tag{22}$$

The eigen-values (λ) of the system matrix are calculated as:

$$\lambda = -c \pm i\sqrt{\frac{-mc^2 + 4k + 4k_e}{4m}} \tag{23}$$

The damping coefficient c in Eq. 19 is obtained using the device quality factor Q as:

$$c = \frac{\sqrt{k/m}}{Q} \tag{24}$$

Substituting c and k_e from Eqs. 16,24) the free-oscillation frequency (also called damped frequency) is simplified to:

$$\omega = \sqrt{\frac{1}{m}[]k(1 - \frac{1}{4Q^2}) - V_L^2 \sum_{j=1}^{9} j a_j q_0^{j-1} - V_L V_D \sum_{j=1}^{9} j b_j q_0^{j-1} + V_D^2 \frac{2.15a}{(q_0 + d)^{3.15}}]} \tag{25}$$

while the natural frequency ω_0 is the oscillation frequency without considering the damping effect which becomes:

$$\omega_0 = \frac{1}{2\pi}\sqrt{\frac{1}{m}[]k - V_L^2 \sum_{j=1}^{9} j a_j q_0^{j-1} - V_L V_D \sum_{j=1}^{9} j b_j q_0^{j-1} + V_D^2 \frac{2.15a}{(q_0 + d)^{3.15}}]} \tag{26}$$

Using Eq. 25, the oscillation period T is then calculated as:

$$T = \frac{2\pi}{\omega} \tag{27}$$

As calculated in [7,11], for a linear system, the double-step command shaping consists of two-step functions in a way that at the end of the first step, the movable electrode experiences a desired displacement (δ) without any residual fluctuations. As shown in Fig. 2, the command parameters are the timing part t_1 and the amplitude part V_{D1} which are defined as the final driving voltage for maintenance at the desired position, the first pulse width, and the first pulse amplitude, respectively. The desired displacement is defined by the user and the required V_{D2} is determined from the experimental data in the characterization process [20]. For the linear system of Eq. 19t_1 and $\widetilde{F}_1$ are calculated as:

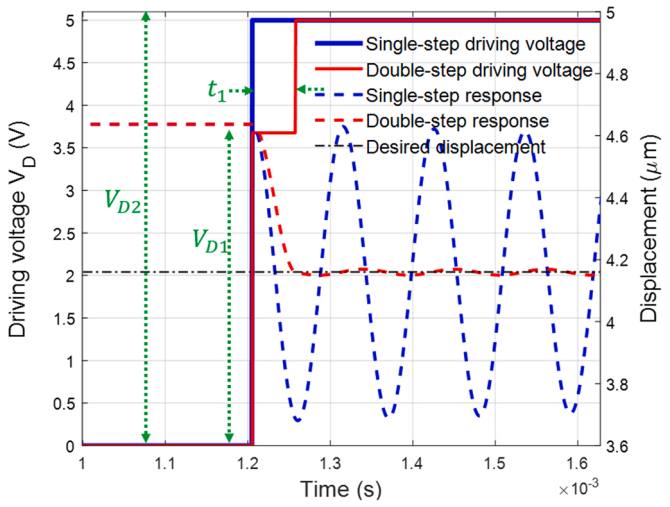

Fig. 2. Simulation of open-loop control using double and single-step command shaping. t_1 and V_{D1} refer to the double-step parameters. The double-step command-shaping is applied for cancelling the residual vibration of the system. The oscillation frequency of the residual vibration mostly happens with the fundamental frequency of the system. The command signal consists of a smaller step for reaching the desired position with zero velocity, and then increasing the driving force to the maintain in the desired position.

$$t_1 = T/2 \tag{28}$$

$$\widetilde{F}(V_{D1}) = (1 - \frac{1}{1 + e^{\frac{\omega_0 t_1}{2Q}}})\widetilde{F}(V_{D2}) \tag{29}$$

Substituting $\widetilde{F}(V_D)$ from Eq. 19 into Eq. 29 gives:

$$B_1 V_{D1}^2 + B_2 V_{D1} = (B_1 V_{D2}^2 + B_2 V_{D2})(1 - \frac{1}{1 + e^{\frac{\omega_0 t_1}{2Q}}}) \tag{30}$$

As a result, V_{D1} is calculated by solving the quadratic algebraic equation in Eq. 30

$$V_{D1} = \frac{1}{2B_1}\left(-B_2 - \sqrt{B_2^2 + 2B_1\widetilde{F}(V_{D2})}\right) \tag{31}$$

4. Experimental setup

A levitation-based MEMS oscillator that includes a micro-cantilever, two fixed side electrodes and a fixed center electrode was fabricated by MEMSCAP using the PolyMUMPS process [28]. Using an optical profiler machine the dimensions fabrication quality and dimensions were checked. The material properties and the design geometry can be found in Table. 1.

The levitation-based MEMS system consists of a micro-cantilever as a movable electrode fabricated at 2 μm above the substrate. Parallel to the movable electrode, a driving electrode was fabricated on the substrate.

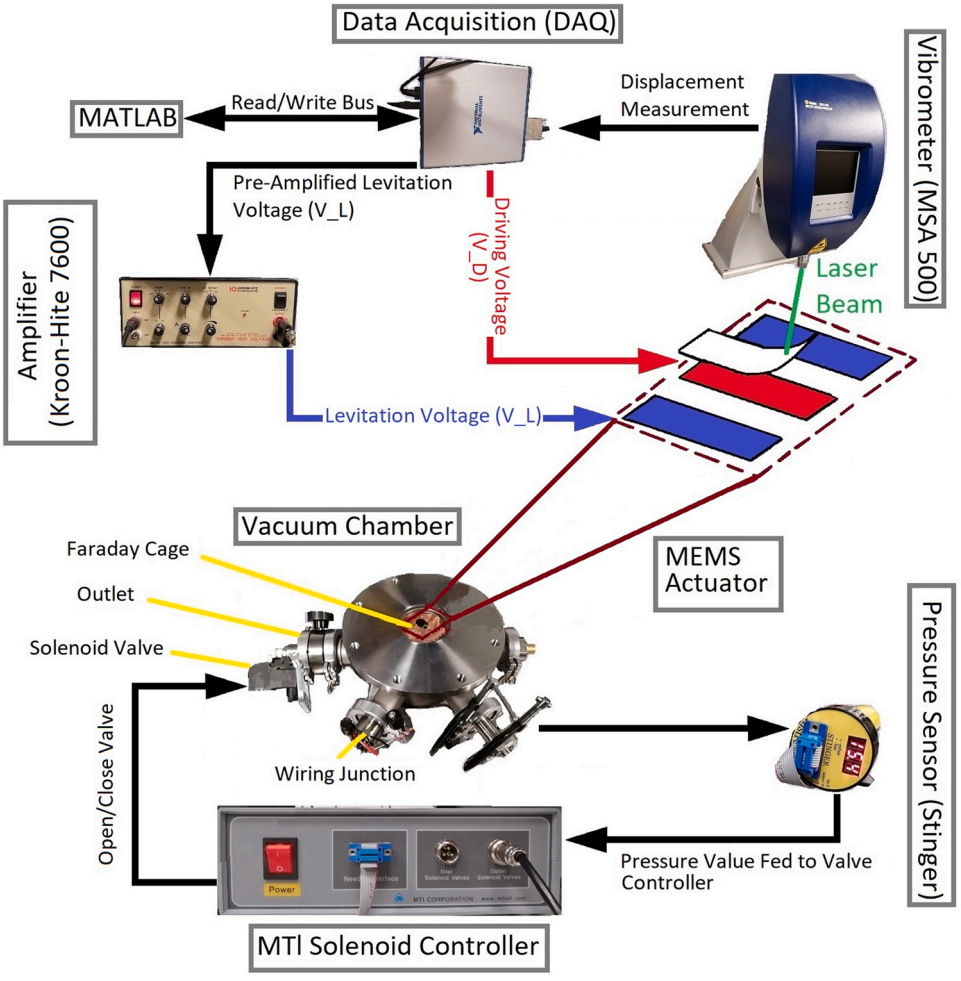

Fig. 3. Experimental setup.

In addition, two electrodes were fabricated at each of the driving electrode which are responsible for applying levitating force to the movable electrode. Table. 1 contains the parameters of the system. According to the PolyMUMPS [28] process, the levitation-based MEMS was fabricated by MEMSCAP. The micro-beam tip displacement and velocity are measured by a laser vibrometer (Polytec MSA-500). The measured data are received and conveyed to MATLAB through a data acquisition system (National Instruments USB 6366 DAQ). The levitating voltage is provided by a wide-band amplifier (Krohn-Hite 7600). A DC power supply (B&K Precision 9110) supplies the driving voltage. The levitating voltage is approximately 10 orders of magnitude greater than the driving voltage. The disparity is caused by the different electrostatic fields, i.e., attraction and levitation at the bottom and the side electrodes, respectively. The voltages are manipulated with MATLAB and the outputs are measured by two electrometers (Keithley 6514) and transferred to MATLAB again through the data acquisition system. The tests were conducted in MEMS and Energy Harvesting Laboratory [29] in 22 °C and relative humidity of 37%. The schematic of the setup is shown in Fig. 3.

The damping ratio that includes structural and air damping was determined according to the experimental results. Using logarithmic decrement, the damping ratio is measured as $\xi = 0.0025$ in $P = 400$ mTorr of air pressure. For pressures larger than 1 Torr, no oscillation is observed which means that the system transient response is overdamped. To demonstrate the effectiveness of the proposed device and method in a severe ring-down situation, the chamber pressure is decreased to 400 mTorr. Squeeze film damping is a resisting force when a fluid is trapped between two solid layers that are in relative motion. This phenomenon is prevalent in MEMS devices and causes mismatch between the linear model and experiments. Considering the levitation MEMS presented in this paper, the movable electrode is levitated away from the substrate and because of the large gap, the air is not highly squeezed. This assumption was proven to be valid because of the close agreement between the simulation and experimental results (see Section 5). Therefore, the linear damping effect properly captures the transient response. The quality factor at the test conditions is obtained as:

$$Q = \frac{1}{2\xi} = 200 \tag{32}$$

5. Results and discussion

In this section, the open-loop control performance applied to a levitation-based parallel-plate mechanism is demonstrated and discussed.Fig. 4.

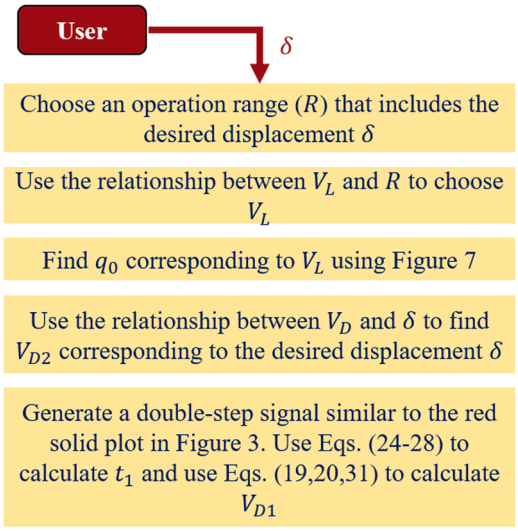

Fig. 4. Open-loop control procedure of the MEMS levitation actuator.

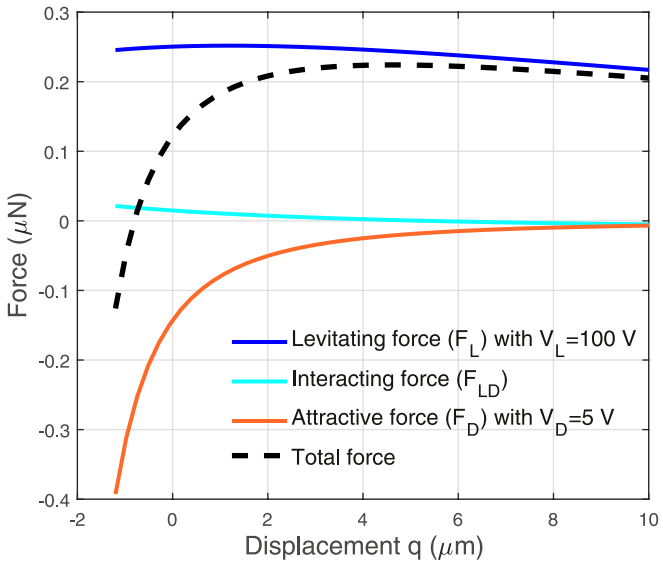

Fig. 5. The variation of the electrostatic force components with the motion of the movable electrode in a levitation MEMS actuator. F_L is the levitating force generated by the side electrodes for the purpose of increasing the operation range. F_D is the driving force generated by the center electrode for the purpose of open-loop position control. F_{LD} is the interacting force generated as a result of the interaction between the side and center electrodes.

5.1. Operation range and linear actuation region

A thorough study of the linearity in the input/output relation is first achieved by force analysis. The experimental and fitting of Multiphysics COMSOL simulation results [19,20] show that the total electrostatic force in levitation MEMS consists of the levitating force F_L, the driving force F_D and the interaction between levitating and driving force F_{LD}. The driving force F_D resembles the parallel-plate capacitive electrostatic force [30] which increases drastically when the movable and the driving electrodes get close to each other. A comparison of the electrostatic force

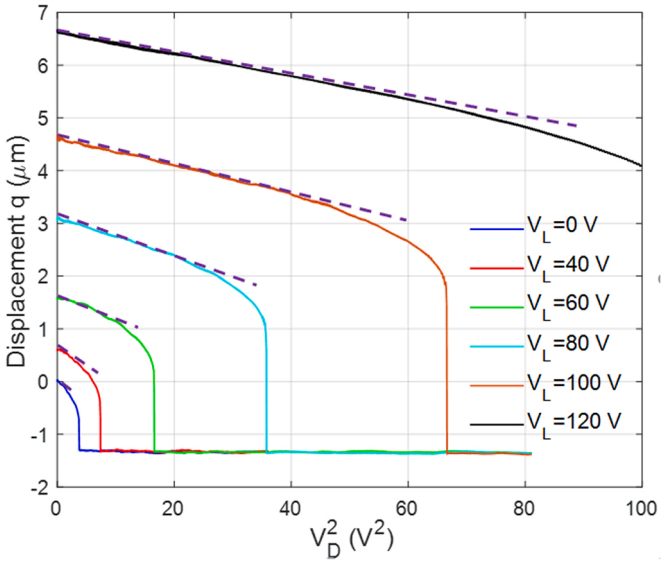

Fig. 6. Static tip displacement of the movable electrode in the presence of different levitating voltages. The linear regions are indicated where the motion is a function of square of the driving voltage V_D only (dashed lines).

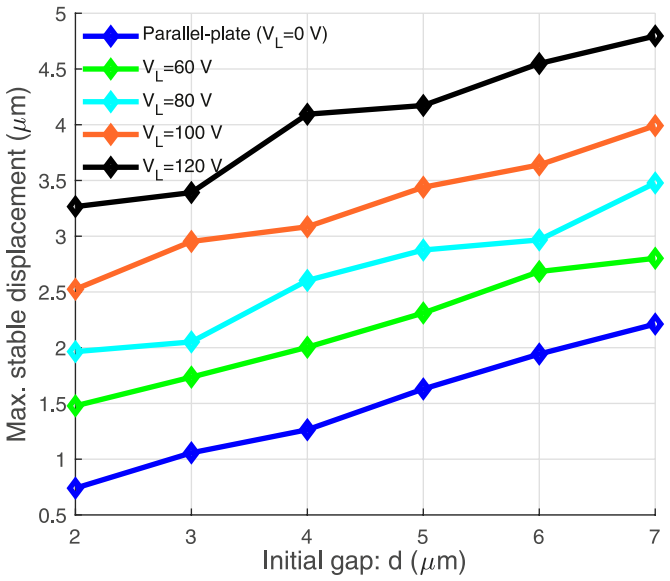

Fig. 7. The effect of the initial gap between the movable electrode and the parallel driving electrode on the maximum stable displacement of MEMS actuators with and without the electrostatic levitation before pull-in instability. The results have been obtained from simulations.

components as a function of the cantilever beam tip displacement is shown in Fig. 5 in the presence of $V_L = 100$ V and $V_D = 5$ V. It is noted that for larger gaps, F_D becomes weaker and mostly insensitive to the variation of the gap with the maximum slope of $2.4 \times 10^{-8} N/per\mu m$. The capacitive force is a nonlinear function of the system state unless there is a sufficiently large gap between the parallel plates [19]. The levitating force F_L and the interacting force F_{LD} varies slightly with the gap where the maximum slope of 5×10^{-9}N/μm observed beyond $4\mu m$. The small slope indicates that the electrostatic force can be considered as a constant force in the system dynamics which is a desirable feature for applying control methods such as double-step linear command shaping [11]. As a result, appropriate regions can be found where the electrostatic force in Eq. 15 is considered as a constant force that varies with inputs V_L and V_D. In the following, the effect of the electrostatic force on the quasi-static response is studied.

As shown in Fig. 6, the static displacement of the movable electrode is plotted versus the square of the driving voltage V_D. The graphs indicate the linear operation range where the driving force is a function of V_D rather than the system state as:

$$Driving\ force = \widetilde{F}(V_D) \approx B_1 V_D^2 + B_2 V_D \tag{33}$$

In this approximation, B_1 and B_2 is considered as a constant value for sufficiently large gaps. This figure also shows the linear input/output relation which is extended in the presence of larger levitating voltage V_L.

A stable operation range is an important design parameter for MEMS devices. For a cantilevered parallel plates mechanism, the initial gap d is defined as the gap between the cantilever tip and the driving electrode. Regarding the range of motion, the movable electrode is driven less than $d/3$ before it collapses due to the pull-in instability. In order to acquire the operation range of R, the initial gap of $d = 3R$ is required. This large gap necessitates a thick sacrificial layer to be released using HF solutions that often causes complications during micro-fabrication processes. The operation range of a MEMS actuator (Table. 1) with the initial gap of d is illustrated in Fig. 7. Fabrication of the levitating electrodes around the driving electrode is a technique to increase the initial gap by inserting a levitating force. As shown in the Fig. 7, the maximum stable displacement in the presence of the levitating voltages $V_L = 60$ V, $V_L = 80$ V, $V_L = 100$ V, and $V_L = 120$ V is plotted versus the initial gap. For $d = 2$ μm, the parallel plates can travel $d = 0.67$ μm, while using the levitating voltage increases this range by 120%, 193%, 277%, and 387% of the gap-closing stable motion range for $V_L = 60$ V, $V_L = 80$ V, $V_L = 100$ V, and $V_L = 120$ V, respectively. The initial gap of $d = 6$ μm provides the operation range of 2 μm. Using the levitating electrodes increases the operation range by 34%, 48%, 82%, and 127% for $V_L = 60$ V, $V_L = 80$ V, $V_L = 100$ V, and $V_L = 120$ V, respectively. The optical angle is twice the mechanical angle of the cantilever tip. Table. 4. This table shows that the optical can be increased 6 times using 120 V of the levitating voltage.

Table 4
The optical angle, drive range, and settling time at different levitating voltages.

Levitating voltage	2-Step drive range	Optical angle
$V_L = 0$ V	0.74 μm	0.17◦
$V_L = 60$ V	1.48 μm	0.34◦
$V_L = 80$ V	1.96 μm	0.45◦
$V_L = 100$ V	2.52 μm	0.58◦
$V_L = 120$ V	3.27 μm	0.75◦

5.2. Double-step command shaping

Unlike gap-closing mechanisms, a unique property of electrostatic levitation is that due to distancing from the substrate and the effect of side electrodes, the electrostatic force becomes a function of the driving voltage and not the gap. This property enables the use of double step command shaping to create a large linear range in the order of micrometers. This is in contrast to gap-closing electrodes where the electrostatic force is a nonlinear function of the gap and the command shaping technique can only be applied to create a small step in the order of nanometers [11,31].

Using command shaping approach for the levitating electrode system, we significantly reduced the ringing in the response of gap-closing electrodes as seen in Fig. 8.b As it can be seen the amount of overshoot and settling times drastically drops. This unique characteristic is very useful for optical switches and modulators.

To investigate the range of motion using the levitating force, we measured and plotted the maximum allowed displacement using the linear double-step command shaping (left axis) as a function of V_L (see Fig. 9). The required driving voltage corresponding to the operation range is shown in the right axis. The conventional gap-closing mechanism allows for the maximum linear travel range of $0.4\mu m$, while applying 80 V, 100 V and 120 V of levitating voltage allows for linear regions as large as 1.15 μm, 2 μm, 2.5 μm, respectively. The required driving voltage for traveling the whole range of motion with $V_L = 80$ V, $V_L = 100$ V and $V_L = 120$ V is 5.5 V, 7.5 V and 11 V, respectively. This result indicates that extending the operation range demands a greater driving voltage. In the following, the achievements regarding the use of command shaping is presented. The settling time was also measured 49 μs, 47 μs, and 46 μs for the displacement of $\delta = 1$ μm in the presence of $V_L = 80$ V, $V_L = 90$ V and $V_L = 100$ V, respectively, which is because the fundamental frequency of the system is higher at higher levitating voltages. Step excitation forces the beam to resonate at its fundamental frequency. The fundamental frequency of the beam was measured to be $f_0 = 9260$ Hz. Using the time response of a linear second-order system actuated by a single-step, one needs to wait for t_s, where

$$1 - 0.96 = e^{-2\pi f_0 \xi t_s} \tag{34}$$

Substituting Eq. 32 in Eq. 34, number of oscillations experienced during the settling time is obtained as:

$$N = \frac{-ln(1 - 0.96)}{\pi} Q = 1.025Q \tag{35}$$

At the operation condition of $P = 400$ mTorr, the Q factor is approximately 200 for the system, and consequently, the user has to wait for 205 oscillations to reach 96% of the desired position. The settling time is linearly increased as the quality-factor is raised. While using double-step

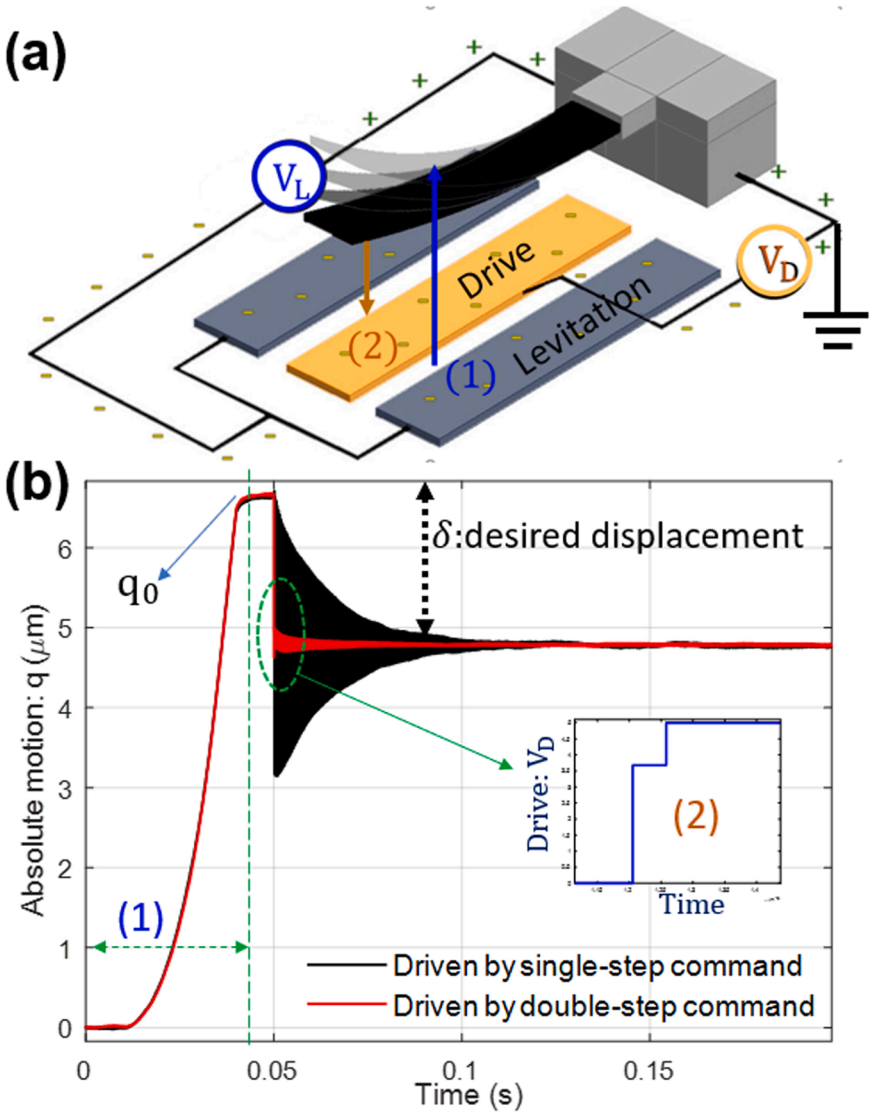

Fig. 8. Part (a): Schematic of open-loop control of levitation-based MEMS actuator. (1) shows the levitation of the micro-cantilever using the levitating electrodes. (2) shows the command shaping driving part using the driving electrode. Part (b): An experimental time history of the open-loop control of a levitation MEMS in the presence of $V_L = 120$ V and q_0 is the initial absolute position at the levitated situation. $\delta = 2$ μm is the desired displacement of the actuator. The red graph shows a single-step drive and the blue graph shows the open-loop controlled motion.

open-loop control reduces the settling time to half of the period, and as a result, the settling time is significantly reduced 400 times.

The open-loop control operation in Fig. 10 demonstrates the driving voltage V_D (left axis) and the displacement ($\delta(t)$) versus time. For the desired displacement of $\delta_0 = 0.5$ μm, the levitating voltages of $V_L = 60$ V, $V_L = 80$ V and $V_L = 100$ V provide the required operation range (see Fig. 9).

The overshoot percentage is evaluated as

$$Over\text{-}shoot\ percentage\ (\%) = \frac{Uncontrolled\ overshoot - residual\ amplitude}{Uncontrolled\ overshoot} \times 100 \tag{36}$$

Compared to the single-step command, the ringdown has been drastically decreased by 98%, 96.5.% and 95.5% of the single-step drive, respectively. Three more tests were conducted for the desired displacement of $1\mu m$ which is allowed for $V_L > 75V$. As a result, 97.5%, 94% and 94% ringdown reduction was observed with the levitating voltages of $V_L = 80$ V, $V_L = 100$ V and $V_L = 120$ V, respectively (see Fig. 10). To explain the residual vibration, the Fast Fourier Transform (FFT) of the residual oscillations in the measured results of Fig. 10 were calculated. A similar peak was observed for different levitating voltages. The dominant frequency is obtained to be 58,823 Hz which is very close to the second mode natural frequency of a cantilever that is calculated as follows:

$$f_{02} = \frac{22.03}{2\pi}\sqrt{\frac{EI}{\rho A L^4}} \tag{37}$$

Using Table. 1, f_{02} in Eq. 37 is 58,171 Hz. The governing partial differential equation Eq. 1 was simplified using only the first mode. Therefore, in contrast with the first mode portion of the step response that is damped using the double-step drive, the dominant mode in the residual fluctuations is the second mode.

To implement the command shaping technique with minimal

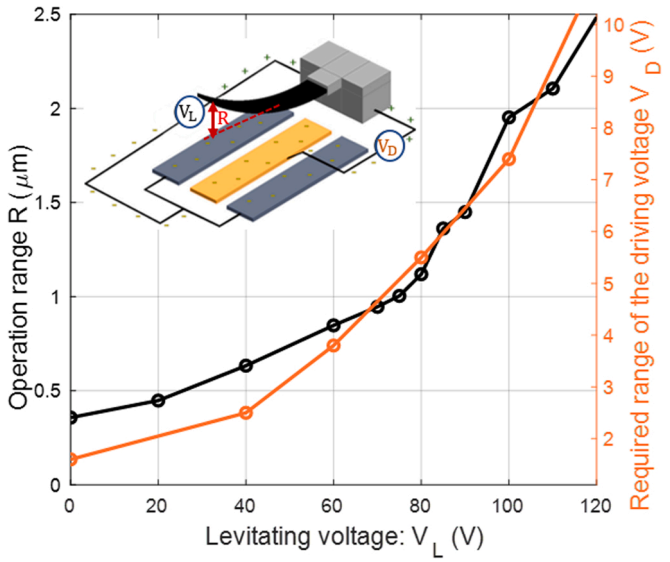

Fig. 9. Left axis: Improvement of the operation range by V_L in the linear driving region (Fig. 6) where the linear command shaping methods are applicable. Right axis: the maximum required driving voltage for travelling the operation range in the presence of V_L.

fluctuations, one needs to obtain the first step magnitude. An analytical solution for to obtain the first step amplitude of the double-step command shaping V_{D1} is shown in Eq. 31. The experimental results of open-loop control with $V_L = 100$ V is compared with the analytical solution in Fig. 11. There is a good agreement for the driving voltages lower than 6 V, while the accuracy is decreased as for large, desired displacements.

The variation of natural frequency due to two step magnitudes causes a challenge in the calculation of accurate timing between the steps to minimize ringdowns. However, this issue is mitigated using the electrostatic levitation. As proved in Eq. 25, the fundamental frequency is varied as the gap is changed. At constant levitating voltages, the variation of fundamental frequency is shown in the left axis of Fig. 12. The right axis of Fig. 12 demonstrates the displacement from the levitated

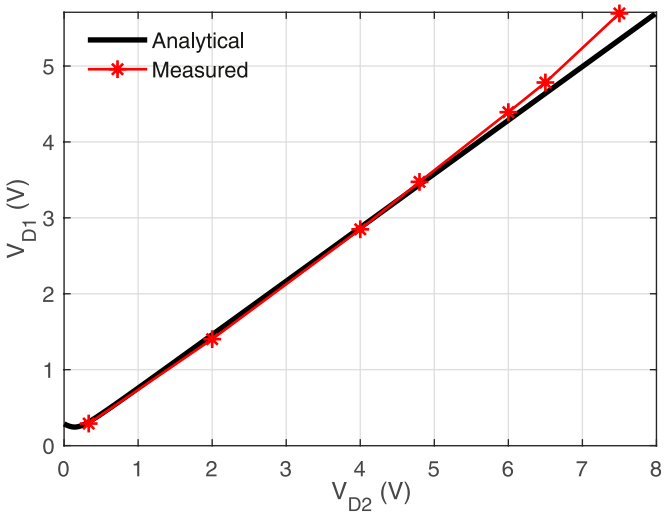

Fig. 11. Amplitude part of the double-step command shaping for verifying the analytical solution using experimental results. x-axis shown refers to the final driving voltage that refers to a desired displacement and y-axis refers to the required driving voltage of the first pulse.

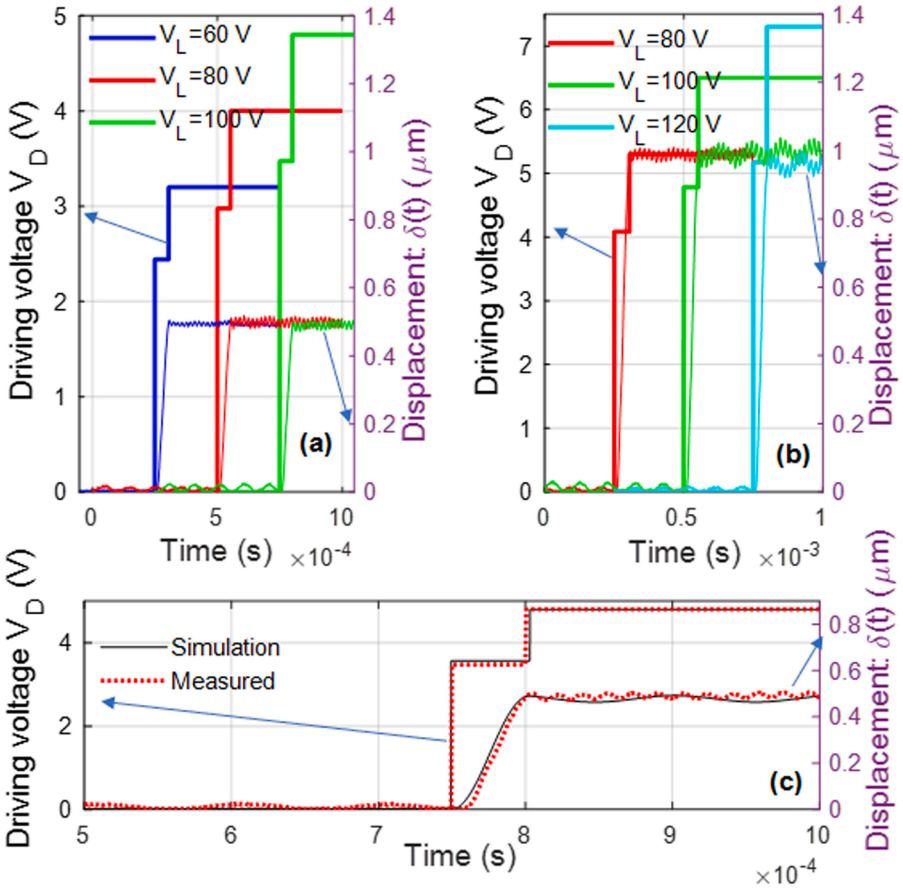

Fig. 10. Part (a): time history (obtained from experiments) of the open-loop control of a levitation MEMS using the double-step command shaping. The double-step signals belong to the left axis which represents the driving voltage V_D. The fluctuating signals represent the displacement of the movable electrode (right axis) that corresponds to the driving voltage of the same color. Part (b): A comparison between the simulation (Eq. 19) and experiments in the presence of $V_L = 100$ V and the desired displacement of 0.5 μm.

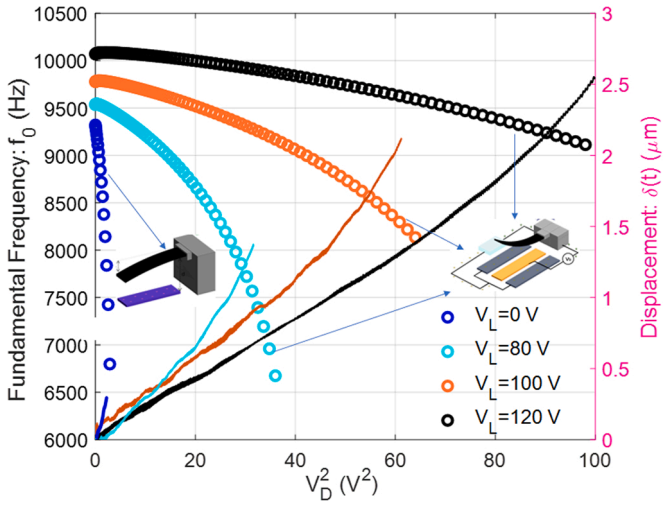

Fig. 12. Left axis: simulation results indicating effect of the driving voltage on the fundamental frequency shift (circle markers). Right axis: measured results showing the static displacement as a function of the square of the driving voltage (solid lines).

position (see Fig. 8). Results show that as V_L is increased, a smaller frequency shift is observed along a wider operation range. The levitating voltages $V_L = 100$ V and $V_L = 120$ V enable the 2 μm and 2.5 μm of operation range, while the frequency shifts of 1500 Hz and 1000 Hz will emerge, respectively. The same value for the conventional gap-closing mechanism is 2500 Hz along a thinner operation range of 0.4 μm. The frequency shift results in an imperfect actuation and increasing the settling time in the open-loop control of MEMS gap-closing drive. By implementing the levitating force, the fundamental frequency becomes less sensitive to the gap-closing electrostatic force that results in a more accurate command shaping.

6. Conclusions

In this research, we overcome the obstacles for the inclusion of small range of motion and nonlinear input to output correlation. The electrostatic levitation is added to the capacitive gap-closing mechanism by the fabrication of two side electrodes. The levitating force raises the movable electrode away from the substrate, which is advantageous because it enables a non-restricted motion in the opposite direction of the substrate and results in an operation range of a multiple of times larger than previous works. Due to the larger distance between the parallel-plates, the relation between the input driving voltage and the gap-closing force becomes linear for a wide range of motion. Such linearity allows for the use of linear command shaping methods such as double-step drive. The linear open-loop control methods are preferred because the command manipulation is simple and only requires the knowledge about the linear stiffness of the movable electrode. The experimental and simulation results show the effectiveness of the double-step command shaping in levitation MEMS actuators. By levitating the movable electrode by 4.5 μm and 6.5 μm, the linear operation range is raised by 5 and 6 times, respectively, compared to the conventional gap-closing mechanism investigated in previous studies. Using the presented results, the idea can be expanded to rotational micromirrors for optical modulation. In addition, more complicated linear command-shaping methods can be implemented for enhancement of the dynamic response.

CRediT authorship contribution statement

Mohammad Mousavi: Conceptualization, formal analysis, Writing – original draft, Writing – review and editing. **Mohammad Alzgool**: Conducting experiments, Data analysis, investigation, Writing – original draft. **Daniel Lopez**: Conceptualization, Supervision, Writing – review and editing. **Shahrzad Towfighian**: Conceptualization, Supervision, Funding acquisition, Writing – review and editing.

Declaration of Competing Interest

The authors declare that they have no known competing financial interests or personal relationships that could have appeared to influence the work reported in this paper.

Acknowledgment

The authors would like to acknowledge the financial support of this study by National Science Foundation (NSF) through Grant #1919608.

References

[1] S.D. Senturia, Microsystem Design, Springer Science & Business Media, 2007.
[2] D.J. Bell, T. Lu, N.A. Fleck, S.M. Spearing, Mems actuators and sensors: observations on their performance and selection for purpose, J. Micromech. Microeng. 15 (7) (2005) S153.
[3] C. Liu, Foundations of MEMS, Pearson Education, India, 2012.
[4] M.K. Mishra, V. Dubey, P. Mishra, I. Khan, Mems technology: a review, J. Eng. Res. Rep. (2019) 1–24.
[5] S.-C. Chen, M.L. Culpepper, Design of a six-axis micro-scale nanopositioner–μ hexflex, Precis. Eng. 30 (3) (2006) 314–324.
[6] M.F. Daqaq, C. Reddy, A.H. Nayfeh, Input-shaping control of nonlinear mems, Nonlinear Dyn. 54 (1) (2008) 167–179.
[7] M. Imboden, H. Han, J. Chang, F. Pardo, C.A. Bolle, E. Lowell, D.J. Bishop, Atomic calligraphy: the direct writing of nanoscale structures using a microelectromechanical system, Nano Lett. 13 (7) (2013) 3379–3384.
[8] L.K. Barrett, T. Stark, J. Reeves, R. Lally, A. Stange, C. Pollock, M. Imboden, D. J. Bishop, A large range of motion 3d mems scanner with five degrees of freedom, J. Micro Syst. 28 (1) (2019) 170–179.
[9] C. Pollock, J. Javor, A. Stange, L. Barrett, D. Bishop, Extreme angle, tip-tilt mems micromirror enabling full hemispheric, quasi-static optical coverage, Opt. Express 27 (11) (2019) 15318–15326.
[10] S.-C. Chen, M.L. Culpepper, S.C. Jordan, J. Danieli, J. Wenger, Application of input shaping and hyperbit control to improve the dynamic performance of a six-axis mems nano-positioner, Engineering (2006).
[11] M. Imboden, J. Chang, C. Pollock, E. Lowell, M. Akbulut, J. Morrison, T. Stark, T. G. Bifano, D.J. Bishop, High-speed control of electromechanical transduction: advanced drive techniques for optimized step-and-settle response of mems micromirrors, IEEE Control Syst. Mag. 36 (5) (2016) 48–76.
[12] C. Pollock, M. Imboden, A. Stange, J. Javor, K. Mahapatra, L. Chiles, D.J. Bishop, Engineered pwm drives for achieving rapid step and settle times for mems actuation, J. Micro Syst. 27 (3) (2018) 513–520.
[13] C. Pollock, L.K. Barrett, P.G. delCorro, A. Stange, T.G. Bifano, D.J. Bishop, Pwm as a low cost method for the analog control of mems devices, J. Micro Syst. 28 (2) (2019) 245–253.
[14] K.-S. Chen, T.-S. Yang, J.-F. Yin, Residual vibration suppression for duffing nonlinear systems with electromagnetical actuation using nonlinear command shaping techniques, J. Vib. Acoust. 128 (6) (2006) 778–789.
[15] K.-S. Chen, K.-S. Ou, Command-shaping techniques for electrostatic mems actuation: analysis and simulation, J. Micro Syst. 16 (3) (2007) 537–549.
[16] C. Bai, J. Huang, Multistep-shaping control based on the static and dynamic behavior of nonlinear optical torsional micromirror, Opt. Eng. 53 (5) (2014), 057109.
[17] Y. Linzon, B. Ilic, S. Lulinsky, S. Krylov, Efficient parametric excitation of silicon-on-insulator microcantilever beams by fringing electrostatic fields, J. Appl. Phys. 113 (16) (2013), 163508.
[18] P.N. Kambali, A.K. Pandey, Nonlinear response of a microbeam under combined direct and fringing field excitation, J. Comput. Nonlinear Dyn. 10 (5) (2015).
[19] M. Pallay, R.N. Miles, S. Towfighian, Merging parallel-plate and levitation actuators to enable linearity and tunability in electrostatic mems, J. Appl. Phys. 126 (1) (2019), 014501.
[20] M. Mousavi, M. Alzgool, S. Towfighian, Electrostatic levitation: an elegant method to control mems switching operation, Nonlinear Dyn. 104 (2021) 3139–3155.
[21] M. Mousavi, M. Alzgool, S. Towfighian, Autonomous shock sensing using bi-stable triboelectric generators and mems electrostatic levitation actuators, Smart Mater. Struct. 30 (6) (2021) 065019, https://doi.org/10.1088/1361-665X/abf72c.
[22] H.M. Ouakad, Static response and natural frequencies of microbeams actuated by out-of-plane electrostatic fringing-fields, Int. J. Non-Linear Mech. 63 (2014) 39–48.
[23] M. Daeichin, M. Ozdogan, S. Towfighian, R. Miles, Dynamic response of a tunable mems accelerometer based on repulsive force, Sens. Actuators A: Phys. 289 (2019) 34–43, https://doi.org/10.1016/j.sna.2019.02.007. ⟨https://www.sciencedirect.com/science/article/pii/S0924424718321149⟩.
[24] M. Mousavi, M. Alzgool, S. Towfighian, A mems pressure sensor using electrostatic levitation, IEEE Sens. J. 21 (17) (2021) 18601–18608.

[25] M. Mousavi, M. Alzgool, S. Towfighian, Enhancing open-loop control of mems using linear electrostatic levitation actuators, IEEE Sens. (2021) 1–4.
[26] M. Pallay, M. Daeichin, S. Towfighian, Dynamic behavior of an electrostatic mems resonator with repulsive actuation, Nonlinear Dyn. 89 (2) (2017) 1525–1538.
[27] O.A. Bauchau, J.I. Craig, Euler-bernoulli beam theory, in: Structural analysis, Springer, 2009, pp. 173–221.
[28] A. Cowen, B. Hardy, R. Mahadevan, S. Wilcenski, PolyMUMPs Design Handbook a MUMPs®process. 2011. Published by MEMSCAP. (http://www.memscap.com/_data/assets/pdf_file/0019/1729/PolyMUMPs-DR-13-0.pdf).
[29] Mems energy harvesting laboratory Binghamton University, Watson School of Engineering & Applied Science Binghamton, New York, U.S.).⟨https://www.binghamton.edu/labs/mems/index.html⟩.
[30] A.H. Nayfeh, M.I. Younis, E.M. Abdel-Rahman, Dynamic pull-in phenomenon in mems resonators, Nonlinear Dyn. 48 (1) (2007) 153–163.
[31] W.-M. Zhang, H. Yan, Z.-K. Peng, G. Meng, Electrostatic pull-in instability in mems/nems: A review, Sens. Actuators A: Phys. 214 (2014) 187–218.

Mohammad Mousavi received his M.Sc. in Mechanical Engineering from the University of Tehran, Iran in 2017. Since 2019, he has started his Ph.D. in Mechanical Engineering department at Binghamton University. His research interests include simulation, dynamic analysis, and motion control of MEMS sensors and actuators. Triboelectric energy harvesting is his second research area.

Mohammad Alzgool received B.Sc. degree in Biomedical engineering and M.Sc. degree in Mechanical engineering from Jordan University of Science and Technology. He has been a Ph.D. student since 2019 in State University of New York at Binghamton since 2019. His areas of interest include MEMS sensors and actuators, modeling, and MEMS fabrication.

Daniel Lopez He received his Ph.D. in Physics from the Instituto Balseiro in Argentina in 1996. After obtaining his Ph.D., he worked as a Postdoctoral Fellow at IBM T. J. Watson Research Center doing research in the field of vortex physics in high-temperature superconductors. Prof. Lopez's research career covered many areas, such as novel materials, nano-mechanics, optical micro-electromechanical systems, and nanofabrication. A common theme in his work has been to use the interplay among materials science, mechanics, and photonics to advance fundamental research and bridge the gap with practical applications.

Shahrzad Towfighian received her Ph.D. degree in Mechanical Engineering from the University of Waterloo,Canada in 2011. She joined the Mechanical Engineering department at Binghamton University in Fall 2013. Her research interests include Micro-electro-mechanical sensors/actuators and energy harvesting. She develops mathematical modeling of electro-mechanical systems to study nonlinearities and their effect on the system performance. She discovers new ways of sensing and actuation for improving functionality of MEMS devices.